Research Square

Preprints are preliminary reports that have not undergone peer review.
They should not be considered conclusive, used to inform clinical practice,
or referenced by the media as validated information.

Geant4 Simulation and Optimization of a Plastic Scintillating Fiber Array: Toward a High-Efficiency Detector for Kr-85 Monitoring

Bin Huang
East China University of Technology
Gui-Ying Guo
Suzhou Nuclear Power Research Institute, Co Ltd
Yan-Jun Huang
hyj1231@163.com

Suzhou Nuclear Power Research Institute, Co Ltd
Jian-Lin Yao
Suzhou Nuclear Power Research Institute, Co Ltd
Qiang-Lin Wei
East China University of Technology
Jin-Min Chen
East China University of Technology
Xue-Dong He
Suzhou Nuclear Power Research Institute, Co Ltd
Yi-Bao Liu
East China University of Technology

Research Article

Keywords: Kr-85, Geant4 simulation, Plastic Scintillating Fiber Array (PSFA), Monte Carlo method, detector optimization, detection efficiency

Posted Date: May 21st, 2026

DOI: https://doi.org/10.21203/rs.3.rs-9572844/v1

License: This work is licensed under a Creative Commons Attribution 4.0 International License.
Read Full License

Additional Declarations: No competing interests reported.

Abstract

To address the need for highly sensitive online monitoring of Kr-85 in gaseous effluents from nuclear facilities, a detection method based on a plastic scintillating fiber array (PSFA) was developed and evaluated using Geant4 Monte Carlo simulation. This study systematically investigated the influence of key structural parameters, including fiber surface polishing, cladding presence, fiber length and diameter, array arrangement, and axial spacing, on the system detection efficiency. The results demonstrate that an optimized configuration employing 410 bare, fully polished fibers (640 μm in diameter, 40 mm in length, spaced 1.12 mm apart axially) without PMMA cladding achieved a theoretical detection efficiency of 71.90%. This configuration provides a performance benchmark for the physical design of a compact, high-efficiency online monitor for Kr-85.

1. Introduction

Krypton-85 is a fission product of U-235, decaying primarily through β-emission (maximum energy 687 keV, branching ratio 99.57%) with a minor γ-ray line at 514 keV (0.43%), and has a half-life of approximately 10.76 years [1]. Monitoring Kr-85 in gaseous effluents from nuclear facilities, such as power stations and reprocessing plants, is a standard regulatory requirement [2, 3]. However, conventional detection methods face inherent limitations. High-purity germanium (HPGe) spectroscopy suffers from high detection limits due to the low γ-ray branching ratio and limited efficiency. Emerging techniques such as atom-trap trace analysis (ATTA) [4] and nanoporous scintillators [5] offer high sensitivity or fast response, but they often require complex vacuum systems or remain at the materials-validation stage. Similarly, liquid scintillation counting (LSC), which targets β-particles, is limited to offline analysis and involves lengthy sample preparation as well as hazardous waste disposal [6, 7]. Therefore, an online monitoring technology that combines high detection efficiency, compact design, and rapid field response is needed to overcome these constraints.

Plastic scintillators are well-suited for online β-monitoring owing to their fast response and adaptability to array configurations. In this work, the Geant4 toolkit is employed[8]; its optical physics models and accuracy in low-energy electron transport have been thoroughly validated[9, 10], providing a reliable foundation for detector design.

Prior studies on fiber-array optimization fall into two main categories. Cheng et al. achieved high sensitivity for tritium detection using hexagonally packed fibers, but their system was restricted to liquid samples and lacked dual-end coincidence[11]. Li et al. realized gaseous tritium detection with unclad fibers, yet the single-end readout limited background rejection [12]. Simulations by Yusoff et al. highlighted critical optical behaviors (edge propagation and crosstalk) that must be considered in gaseous applications [13]. Although Zeng et al. successfully detected Kr-85 with a phoswich detector employing anti-coincidence logic, the near-absence of γ-rays in Kr-85 decay makes β-γ coincidence strategies inherently inefficient [14].

To address these gaps, we propose a novel bare-plastic-scintillator-fiber array for Kr-85 monitoring, operated in dual-PMT coincidence mode. This design replaces toxic liquid scintillators with solid scintillating fibers and uses dual-end timing to suppress random noise, making it suitable for complex field environments [11]. The system allows direct gas injection for real-time analysis, eliminating the delay and potential bias of offline sampling.

Methodologically, this study employed Geant4 to simulate an array of 410 unclad polystyrene fibers housed in a copper chamber coupled to R1924A photomultiplier tubes. Key parameters, such as surface treatment, cladding presence, and geometric layout, were optimized to approach the theoretical sensitivity limit. By focusing on computational physics, this work establishes the performance ceiling of the proposed technology and discusses the practical challenges involved in translating the simulated design into physical hardware.

2. Materials and Methods

2.1 Simulation Tool and Physics Processes

In this work, the G4EmLivermorePhysics electromagnetic physics list was employed to simulate the transport of low-energy β-particles [15]. This list incorporates an electron energy cutoff as low as 100 eV and models essential processes such as ionization, excitation, multiple scattering, bremsstrahlung, fluorescence, and Auger electron emission. These processes are critical for performing fine-grained energy deposition calculations of Kr-85 β-particles, which have a mean energy of approximately 250 keV. The simulations were conducted using the Geant4 toolkit (version 11.1.3), which incorporates recent advancements documented by Allison et al., including advanced electromagnetic physics models and multithreading capabilities that improve simulation efficiency for complex detector geometries[16].

Optical processes were simulated using the *G4OpticalPhysics* module [10]. The module handles the generation of scintillation photons (with a polystyrene light yield of 8000 photons/MeV, a decay time of 2.7 ns, and an emission peak at 492 nm), their propagation within the fiber core, total internal reflection and refraction at interfaces, and finally, absorption at the photomultiplier tube (PMT) photocathode, all based on geometric optics theory. The optical interfaces of the scintillating fibers were modeled with the *G4OpticalSurface* class using the unified model. A polished finish was applied in the baseline configuration to ensure specular reflection. For comparative studies evaluating the effect of surface roughness, a ground finish with a Lambertian angular distribution was adopted.

To establish the dual-PMT coincidence measurement model, sensitive detectors were defined at both photocathodes to record photon hit counts per event. In post-processing, these hits were converted to photoelectron numbers using the quantum efficiency curve of the Hamamatsu R1924A PMT (peak efficiency ~ 22% at 420 nm). The coincidence criterion required that, for the same primary particle event, both PMTs register at least one photoelectron within a 20 ns time window. The selection of this 20 ns window is informed by the systematic study of Zhu et al. on dual-end coincidence detectors using EJ-

200 plastic scintillators [17]. Their experimental work demonstrated that detection efficiency saturates once the coincidence window exceeds 10 ns. Considering the scintillator decay time (on the nanosecond scale), the PMT transit-time spread (TTS ≈ 1.17 ns), and electronic timing resolution, they determined an optimal online coincidence window of 16 ns. The 20 ns window adopted in this work is a conservatively relaxed value based on that reference, accounting for the specific plastic scintillating fiber decay time (2.7 ns), photon transit time fluctuations (< 1 ns), and the PMT TTS (≈ 1.5 ns). This ensures genuine coincidence signals are retained while effectively rejecting accidental background. The feasibility of dual-end coincidence for event discrimination in such detectors is further supported by the work of Pi et al. [18]. Only events satisfying this coincidence criterion were counted as valid detections, thereby simulating an electronic coincidence circuit and enabling the quantitative evaluation of the system's overall detection efficiency.

2.2 Detector Geometric Model and Materials

The overall detector structure is illustrated in Fig. 1, which shows both the simulation model and a photograph of the physical device. The core sensing element is a plastic scintillating fiber array (PSFA). A detailed view of the basic simulation geometry is provided in Fig. 2. The initial baseline model was constructed with the following components and parameters:

(1) Scintillating Fiber

A single scintillating fiber consists of a cylindrical polystyrene core and a concentric polymethyl methacrylate (PMMA) cladding. The core has a density of 1.05 g/cm³ and a refractive index of 1.60 at 492 nm (the emission peak), a key parameter for calculating total internal reflection in Geant4. The PMMA cladding has a density of 1.18 g/cm³ and a refractive index of 1.49, providing a fixed refractive-index contrast with the core. In the simulation, the core material is assigned a light yield of 8000 photons/MeV, a scintillation decay time of 2.7 ns, and an emission peak at 492 nm. The refractive-index difference enables total internal reflection. A minimum photon-trapping efficiency of 3.44% is configured to restrict photons within the core for efficient axial transmission. Optical boundary processes—including transmission, reflection, and absorption—are activated at the core–cladding interface to accurately simulate photon propagation.

(2) Plastic Scintillating Fiber Array (PSFA)

The initial design employs a hexagonal close-packed arrangement of 367 scintillating fibers. Each fiber has a core diameter of 960 μm and a 20 μm-thick PMMA cladding. The array is fixed at both ends by PMMA plastic disks (2 mm thick, 27 mm in diameter, sized according to the fiber spacing and diameter), forming a detection array with an effective length of 60 mm.

(3) Detection Chamber

The PSFA is housed in a cylindrical pure-copper chamber that provides electromagnetic shielding. Both ends of the chamber are coupled to Hamamatsu R1924A photomultiplier tubes (PMTs) via aluminum-

alloy sleeves; the PMT photocathode diameter is set to 22 mm. Silicone sealant ensures optical and gas sealing between the PMTs and the chamber body. Fluorinated silicone oil is applied at the interface between the PMT window and the PSFA end face to achieve high-efficiency optical coupling.

(4) Source Volume

In the simulation, the interstitial spaces within the PSFA inside the detection chamber are filled with a uniform distribution of the Kr-85 gas to be measured.

2.3 Source Definition and Particle Emission

The β-particle energy spectrum of Kr-85 used in the simulation is shown in Fig. 3. The radioactive source is modeled as Kr-85 gas uniformly distributed within the detection chamber's gas volume. The decay process is simulated by generating β particles according to the actual Kr-85 β spectrum, which has an endpoint energy of 687 keV and a mean energy of 251 keV. The accompanying 514 keV gamma ray, with a very low branching ratio of 0.43%, is omitted from the present and all subsequent simulations. This simplification is justified because the contribution of gamma-ray events to the total signal is negligible (less than 0.5% of β-induced events) and its exclusion does not affect the optimization of detector parameters for the dominant β particles. Including the gamma ray would unnecessarily increase the computational complexity without providing meaningful insight for the design objectives. To ensure acceptable statistical uncertainty, each simulation run is performed with 10^6 primary particle events.

2.4 Simulation Parameters and Performance Metrics

The primary objective of the simulation is to calculate and optimize the overall detection efficiency, ε, of the Kr-85 detection system. The detection efficiency is defined as the ratio of the number of events effectively recorded by the detector to the total number of primary particle decays simulated. An event is considered valid based on the dual-PMT coincidence principle: it is counted only if, within the same primary particle event, the photocathodes of both PMTs record at least one photoelectron. This criterion mimics an electronic coincidence circuit and is designed to suppress single-PMT noise effectively.

A key performance metric for the detector is the minimum detectable concentration (MDC), which is calculated using the following formula derived from the Currie equation [19]:

$$MDC = \frac{4.65\sqrt{n_b/t_b}}{\varepsilon \cdot V \cdot \eta} \qquad (1)$$

where n_b is the background count rate (cps), t_b is the background counting time (s), assumed equal to the sample counting time, V is the sample gas volume (m^3), η is the gas recovery efficiency (temporarily set to 1 in this simulation, though practical systems require gas-path optimization to approach this value), and ε is the detection efficiency. In this simulation phase, the main focus is to maximize ε by

optimizing the geometric parameters, thereby theoretically lowering the *MDC*. Assuming representative operational parameters (n_b = 0.3 cps, t_b = 3600 s, V = 0.010 m³, η = 1), the optimized theoretical *MDC* reaches approximately 5.9 Bq/m³. This result demonstrates the feasibility of achieving high sensitivity with a compact detector design.

2.5 Simulation Optimization Scheme

To achieve optimal system detection efficiency, this study systematically simulated the influence of several key structural parameters. The specific optimization procedure is outlined as follows:

(1) Surface Optical Treatment

The effect of surface finish on photon transmission efficiency was evaluated by comparing two interface conditions: a "polished" state (representing an ideal smooth optical interface) and an "unpolished" state (characterized by significant diffuse reflection). This comparison was applied to both the fiber-core/PMMA-cladding interface and the PMMA-cladding/Kr-85 gas interface.

(2) PMMA Cladding Thickness

The combined influence of PMMA cladding thickness on β-particle penetration and scintillation photon confinement was investigated. Simulations were performed for cladding thicknesses ranging from 0 μm (i.e., a bare fiber with no cladding) up to several tens of micrometers.

(3) Fiber Length

Fiber length was varied from 20 mm to 100 mm to examine the trade-off between the probability of β-particle energy deposition and the scintillation photon self-absorption effect.

(4) Fiber Diameter

The diameter of a single fiber core (without cladding) was adjusted to evaluate its impact on particle-interaction cross-section and scintillation photon collection efficiency.

(5) Array Arrangement and Spacing

Different array configurations—such as hexagonal and circular packing—were compared. The axial spacing between adjacent fibers was also adjusted to optimize the packing fraction of the fiber array and the spatial utilization within the fixed chamber volume.

3. Results and Discussion

Building on the Geant4 model established in Section 2, this section employed a sequential, one-factor-at-a-time optimization approach. Each key structural parameter was optimized by controlling other variables, after which the overall configuration was verified to obtain the theoretically optimal detector design. This optimization strategy follows the methodology developed by Cheng et al. for plastic

scintillating fiber (PSF) array tritium detectors in aqueous media[20]. In their work, parameters such as fiber radius, length, and array structure were varied sequentially to maximize detection efficiency. Furthermore, Xu et al. validated through Geant4 simulation that inner-wall polishing significantly enhances photoelectron yield in drilled-hole plastic scintillator detectors[21]. Their results show that polished surfaces achieve substantially higher photon collection efficiency than ground surfaces, a conclusion consistent with the interface treatment findings presented in Section 3.1 of this paper.

The sequence of optimization in this work is determined by the physical coupling strength among parameters. Surface treatment and cladding are optimized first, followed by geometric dimensions (length and diameter), and finally array arrangement parameters (shape and spacing). The latter are addressed last due to their dependence on the spatial configuration defined by the earlier parameters. This order aligns with the logic employed in the studies cited above, which prioritize optimizing single-fiber energy deposition and photon transmission before addressing array-level packing and spatial efficiency.

3.1 Influence of Surface Optical Treatment on Detection Efficiency

The simulation first investigated the critical influence of the optical surface treatment of the plastic scintillating fiber on the system's detection performance. In the baseline detector model, scintillation photon transmission involves two main material interfaces: the interface between the plastic scintillator core and the PMMA cladding (Interface 1), and the interface between the PMMA cladding and the Kr-85 gas (Interface 2). For a fiber core diameter of 0.96 mm, a PMMA cladding thickness of 20 μm, a center-to-center fiber spacing of 1.1 mm, and a hexagonal array arrangement, the effect of polishing these two interfaces on the system detection efficiency was examined.

Two extreme cases were compared: both interfaces were set as "polished" (ideal smooth optical interface) or both as "unpolished" (with strong diffuse scattering). The results presented in Table 1 demonstrate that the optical state of the interfaces has a profound impact on detection efficiency. When both interfaces are unpolished, scintillation photons undergo severe diffuse scattering at each interface, preventing effective confinement of photons within the fiber core for axial transmission. Consequently, the probability of photons reaching the PMT photocathode drops sharply, yielding a system detection efficiency of only about 5.81%—rendering effective detection nearly impossible. In contrast, when both interfaces are polished, photons experience total internal reflection or specular reflection, which greatly enhances axial photon transmission along the fiber. Under the same geometric configuration, the system detection efficiency rises sharply to 42.56%.

Because photons must propagate sequentially through Interface 1 and Interface 2, diffuse scattering at either interface disrupts photon confinement, randomizes the transmission path, and leads to severe optical loss. This observation aligns with the Geant4 simulation results of Xu et al. for drilled-hole plastic scintillator detectors, in which inner-wall polishing significantly enhanced photoelectron yield compared

to unpolished surfaces [21]. Their finding further confirms the critical role of interface optical treatment in PSF-type detectors.

Table 1
Detection efficiency under different surface optical treatment conditions.

Interface 1	Interface 2	Efficiency(%)
Polished	Polished	42.56
Unpolished	Polished	5.81
Polished	Unpolished	5.81
Unpolished	Unpolished	5.81

These results unequivocally demonstrate that high-quality optical treatment of fiber interfaces is a prerequisite for achieving viable detection efficiency in PSFA-based radiation detectors. Diffuse scattering randomizes the photon path, increases the probability of photon absorption, and thereby causes severe optical signal loss. Therefore, in practical detector fabrication, it is essential to select high-quality scintillating fibers with smooth surfaces. During assembly, optical coupling agents should be used to ensure good optical contact between the fiber end-face and the PMT photocathode, thereby minimizing interfacial signal loss. This result also indirectly questions the feasibility of complex scintillator geometries (such as "drilled-hole" types) whose internal surfaces are difficult to polish effectively.

3.2 Optimization and Trade-off of PMMA Cladding Thickness

The PMMA cladding layer is designed to serve as a reflective interface, confining scintillation photons within the fiber core to improve photon transmission efficiency. Nevertheless, β particles must first penetrate the cladding before reaching and depositing energy in the scintillator core; consequently, the cladding thickness inevitably attenuates incident β particles.

To quantify the trade-off between these two competing effects, the system detection efficiency was simulated for PMMA cladding thicknesses of 0, 10, 20, 30, 40, and 50 μm, with all other parameters fixed (core diameter 960 μm, polished interfaces, hexagonal array). The simulation results are presented in Fig. 4. As shown in Fig. 4b, the detection efficiency decreases monotonically as the cladding thickness increases. Even a 10 μm PMMA cladding significantly reduces the efficiency compared with the bare-fiber (0 μm cladding) case. When the PMMA cladding is completely omitted, the system attains its maximum detection efficiency under otherwise identical conditions. This trend indicates that, for Kr-85 β particles, the attenuation effect of the PMMA cladding on incident particles outweighs its optical confinement benefit.

Figure 4a provides the underlying photon statistics that explain this efficiency trend. The effective coincidence photon spectra—representing the distribution of total photon counts recorded simultaneously by both PMTs within the 20 ns coincidence window—evolve systematically with cladding thickness. The bare-fiber configuration (black curve) shows the broadest spectral distribution and the largest integrated area, corresponding to the highest detection efficiency. Although its spectral peak is not the tallest, the distribution extends furthest toward high photon numbers (up to ~ 1200 photons), reflecting abundant scintillation photon production in the polystyrene core and efficient axial transmission in the absence of cladding attenuation.

As the cladding thickness increases, the spectra progressively narrow and shift toward lower photon counts: 10 μm (red curve, peak ~ 21,000 counts at ~ 35 photons), 20 μm (blue curve, peak ~ 19,000 counts at ~ 40 photons), 30 μm (green curve, peak ~ 17,500 counts at ~ 45 photons), 40 μm (purple curve, peak ~ 16,500 counts at ~ 50 photons), and 50 μm (yellow curve, peak ~ 15,000 counts at ~ 55 photons). It is noteworthy that the 10 μm and 20 μm curves exhibit slightly higher peak counts than the bare-fiber curve, yet their integrated spectral areas are substantially smaller. This indicates significantly fewer total coincidence events, a result of β-particle attenuation in the cladding. The spectral evolution directly reflects the reduction in β-particle energy deposition within the scintillator core as cladding thickness increases: fewer scintillation photons are generated, the photon-count distribution contracts toward lower values, and consequently the number of events satisfying the dual-PMT coincidence threshold decreases.

These findings align with the experimental work of Chu et al., who demonstrated continuous gaseous-tritium measurement capability using unclad plastic scintillating fiber arrays, achieving a detection efficiency of approximately 9%[4]. Although their geometry differed from the present design, their validation of unclad fibers for gaseous β-emitter detection supports the conclusion drawn here.

3.3 Optimization of Fiber Geometric Dimensions

Following the conclusion that bare fibers (without PMMA cladding) maximize detection efficiency (Section 3.2), this section optimizes the two key geometric parameters of the scintillating fibers: length and diameter. All simulations in this section use bare polystyrene fibers (no cladding) with a core diameter of 960 μm, arranged in a hexagonal close-packed array of 367 fibers with 1.1 mm axial spacing, unless otherwise stated.

3.3.1 Fiber Length

The system detection efficiency was simulated for fiber lengths ranging from 20 mm to 100 mm, with all other parameters held constant. Results are shown in Fig. 5. As seen in Fig. 5b, the efficiency rises rapidly from 55.31% at 20 mm to a peak of 55.79% at 40 mm, after which it declines monotonically to 53.84% (60 mm), 52.60% (80 mm), and 48.70% (100 mm). This trend results from the competition between two physical effects: (i) the gain in energy deposition probability as fiber length increases, which reduces the chance of β-particle escape and enlarges the effective detection volume; and (ii) the

loss in photon collection efficiency at greater lengths, where increased transmission distance lowers the probability of successful dual-PMT coincidence.

Figure 5a provides the corresponding photon statistics. The effective coincidence photon spectra show a clear evolution with length. The 40 mm configuration (red curve) exhibits the broadest distribution, extending to high photon numbers, which indicates efficient energy deposition and favorable photon transmission. For lengths beyond 40 mm, the spectra shift progressively leftward and their peaks increase: 60 mm (blue, ~ 18,000 counts), 80 mm (green, ~ 38,000 counts), and 100 mm (purple, ~ 57,000 counts) display higher, narrower peaks. This shift reflects increased self-absorption and transmission losses during longer-distance photon propagation, which reduces the average photon count per event. The 20 mm configuration (black curve) has a lower peak (~ 5,000 counts) than the 40 mm case, primarily because its shorter length allows many β particles to traverse the fiber without depositing their full energy. Nevertheless, it still outperforms the 80 mm and 100 mm cases, confirming that transmission losses dominate at greater lengths.

The optimal length of 40 mm arises from the balance between these competing factors. For Kr-85 β particles, a 20 mm fiber is too short to ensure complete energy deposition, whereas at 40 mm the probability of full energy deposition approaches saturation while photon transmission losses remain small (the attenuation length of polystyrene at 492 nm is typically 1–4 m, far exceeding 40 mm). Beyond 40 mm, however, the dual-PMT coincidence probability becomes the limiting factor: photons generated near the fiber center must travel roughly 20 mm to reach either PMT, and statistical fluctuations in photon partitioning between the two ends increase the chance that one PMT records no photoelectron, thereby reducing coincidence efficiency. This loss outweighs the marginal further gain in energy deposition probability, causing the net efficiency to drop.

Therefore, 40 mm is identified as the optimal fiber length for this detector configuration, balancing improved β-particle energy deposition against reduced coincidence probability due to photon transmission and partition effects.

3.3.2 Fiber Diameter

With other parameters fixed (bare fiber, length 40 mm, hexagonal array of 367 fibers, 1.1 mm axial spacing), the influence of fiber diameter on detection efficiency was evaluated. Results are presented in Fig. 6. Figure 6b shows that efficiency remains relatively high in the range of 580–700 μm, reaching a broad peak of about 63% at 640 μm. Outside this range, efficiency declines monotonically, falling to approximately 53% at 1000 μm. Even the smallest diameter tested (520 μm) achieves an efficiency of 62.53%.

The effective coincidence photon spectra in Fig. 6a (inset shows a magnified view of the 0–200 photon region) reveal that all diameters produce similar spectral shapes in the low-photon region, with peaks clustered between 40 and 60 photons. However, subtle differences appear in the high-photon tail: the 640 μm configuration shows a slightly broader distribution extending to higher counts, reflecting

marginally better energy deposition and photon collection. As diameter increases beyond 640 μm, the spectra gradually narrow and shift leftward, indicating greater photon transmission losses and reduced coincidence probability because photons must travel longer average path lengths within thicker fibers.

The existence of an optimal diameter range stems from the interplay between particle interception and photon transport at the single-fiber level. For Kr-85 β particles, the probability of a particle intersecting a fiber core exceeds 90% for diameters above 500 μm, as the fiber diameter is comparable to the particle range. Consequently, particle-interception probability is nearly saturated across the entire tested range (520–1000 μm), and efficiency variations are dominated by photon-transport effects. In thicker fibers (diameter > 700 μm), scintillation photons generated near the core center must travel a greater distance to reach the fiber surface and experience total internal reflection, increasing the chance of bulk absorption and scattering. This lowers the average photon count per event and degrades the dual-PMT coincidence probability. Moreover, larger diameters occupy more volume within the fixed chamber, reducing the total number of fibers and the array's surface-area-to-volume ratio, which slightly decreases the overall β-particle interaction probability.

A diameter of 640 μm is therefore selected as optimal, representing the best compromise between maintaining high particle-interception efficiency and minimizing photon-transport losses. The broad efficiency plateau (580–700 μm) provides practical manufacturing tolerance, allowing for typical fiber-diameter variations without significant performance degradation.

3.4 Optimization of Fiber Array Arrangement

3.4.1 Arrangement Shape and Fiber Number

With the optimal bare-fiber configuration established (length 40 mm, diameter 640 μm), this section investigates the combined influence of array-packing geometry and fiber number (equivalent to layer number) on detection efficiency. Three close-packed arrangements—hexagonal, octagonal, and circular—were compared under identical boundary conditions: chamber inner diameter 27 mm, fiber diameter 640 μm, and axial spacing 1.10 mm. The results are presented in Figs. 7 and 8, which provide complementary views of the simulation outcomes.

Figure 7 examines the dependence on layer number. Panels 7a–7e display the effective coincidence photon spectra for the three arrangements at 6 to 10 layers. At 6–7 layers (Figs. 7a–b), the three arrangements exhibit comparable spectral shapes, with the hexagonal arrangement showing a slight advantage due to its higher intrinsic packing density. As the layer number increases to 8–10 layers (Figs. 7c–e), the circular arrangement progressively outperforms the others, reaching the highest spectral peak at 10 layers (~ 15,000 counts for circular vs. ~13,000 for hexagonal). This crossover reflects a boundary-truncation effect: at higher layer numbers, the hexagonal and octagonal arrangements suffer increasingly severe truncation at the circular chamber boundary, producing partial peripheral fibers with compromised optical coupling. The circular arrangement, owing to its radial symmetry, maintains complete fiber integrity across all layers, thereby minimizing edge losses.

Figure 7f quantifies this layer-dependent trend using a radar chart. The circular arrangement shows a steep rise in efficiency from 6 to 10 layers, whereas the hexagonal arrangement plateaus and the octagonal arrangement consistently lags.

Figure 8 presents the results from a fiber-number perspective, together with visual confirmation of the array geometries. Panels 8a–b (circular), 8c–d (hexagonal), and 8e–f (octagonal; note that an octagonal layout cannot accommodate 11 full layers, hence it is shown only up to 10 layers) show the effective coincidence photon spectra and efficiency-versus-fiber-number curves, respectively. Efficiency increases monotonically with fiber number for all arrangements, but the circular arrangement achieves the highest peak efficiency at 410 fibers (11 layers), which corresponds to the maximum chamber filling without boundary truncation. Panels 8g–i provide schematic views of the three layouts at their respective maximum fiber numbers, clearly illustrating the boundary-matching advantage of the circular arrangement (8g: complete circular filling) compared to the truncated edges of the hexagonal (8h) and octagonal (8i) layouts.

The circular arrangement with 11 layers (410 fibers) is therefore selected as the optimal array configuration. This choice is justified by its geometric compatibility with the cylindrical chamber boundary at high packing densities, which eliminates edge-truncation losses and maximizes the effective detection volume. The efficiency advantage of the circular arrangement becomes apparent only when the layer number exceeds a boundary-matching threshold (around 8 layers); below this threshold, the hexagonal arrangement's higher packing density dominates.

3.4.2 Fiber Axial Spacing

Using the optimal fiber dimensions (bare fiber, diameter 640 μm, length 40 mm) and array arrangement (circular, 410 fibers), the system detection efficiency was further optimized by fine-tuning the axial spacing (center-to-center distance) between adjacent fibers. The spacing was varied from 1.06 mm to 1.13 mm in steps of 0.01 mm, with all other parameters fixed. The results are shown in Fig. 9.

Figure 9b indicates that detection efficiency increases monotonically from 66.79% at 1.06 mm to a peak of 71.90% at 1.12 mm, then decreases slightly to 71.51% at 1.13 mm. Notably, efficiency exhibits a broad plateau in the range 1.10–1.12 mm (approximately 70.8%–71.9%), indicating robust performance that is insensitive to minor spacing variations within this range. This plateau provides practical tolerance for array assembly.

Figure 9a provides the underlying photon statistics. The effective coincidence photon spectra (inset shows a magnified view of the 0–200 photon region) are similar for all spacings, with the 1.12 mm configuration displaying the broadest distribution. The subtle differences in spectral amplitude reflect a trade-off between fiber packing density and gas volume: at smaller spacings, higher fiber density improves β-particle interception probability but reduces the Kr-85 gas volume, thereby decreasing the total radioactive source available; at larger spacings, the expanded gas volume increases the source

quantity but lowers fiber density, raising the probability that β particles traverse the inter-fiber gaps without interaction.

An axial spacing of 1.12 mm is therefore selected as optimal, achieving the highest detection efficiency by balancing the "porosity" of the fiber array: sufficient Kr-85 gas volume for β-particle generation and transport, and adequate fiber density for efficient particle interception and photon collection. The broad efficiency plateau (1.10–1.12 mm) accommodates practical assembly tolerances.

3.5 Final Optimized Configuration and Theoretical Performance

3.5.1 Optimal Parameter Set

By integrating the results of the stepwise parameter optimization described in the preceding sections, this simulation study yields a theoretically optimal set of physical design parameters for the PSFA-based Kr-85 detector, as summarized in Table 2. The core parameters are as follows:

Fiber Type: Bare plastic scintillating fiber (no PMMA cladding) with a polished surface.

Fiber Dimensions: Diameter 640 μm, length 40 mm.

Array Structure: 410 fibers arranged in a close-packed circular pattern, with an axial (center-to-center) spacing of 1.12 mm.

Optical Requirement: All critical optical interfaces (fiber surfaces, fiber end faces, and PMT windows) must be smooth and achieve high-efficiency optical coupling.

3.5.2 Theoretical Detection Efficiency

As indicated in Table 2, the Geant4 simulation predicts a total system detection efficiency (ε) for Kr-85 of 71.90% under the above optimal configuration. This value represents the probability that a Kr-85 β-decay event within the detector chamber generates sufficient scintillation photons to trigger the dual-PMT coincidence system. It encompasses the complete chain of β-particle energy deposition, scintillation photon generation and propagation, and photon arrival at the photocathodes.

It is important to note that this 71.90% efficiency is derived from Monte Carlo particle transport including optical photon tracking. The practical system efficiency will be lower due to additional factors such as the PMT quantum efficiency, electronic threshold effects, and optical coupling losses. The selected Hamamatsu R1924A PMT, with its bialkali photocathode and spectral response covering 300–650 nm, provides adequate sensitivity at the polystyrene emission peak (492 nm). Prototype validation is required to determine the actual electronic detection efficiency.

Table 2
Summary of optimized detector structural parameters.

Parameter/Condition	Initial Value	Comparison values	Optimized value
Polishing?	Ture	True or False	True
PMMA Cladding	20μm	0、10、20、30、40、50(μm)	0μm
Fiber Length	60mm	20、40、60、80、100(mm)	40mm
Fiber Diameter	960μm	520、580、640、700、760、820、880、940、1000(μm)	640mm
Fiber Arrangement	hexagonal distribution	circular distribution、hexagonal distribution、ctagonal distribution	circular distribution
Axial Spacing	1.1mm	1.06、1.07、1.08、1.09、1.1、1.11、1.12、1.13(mm)	1.12
Fiber Number	367	130、173、223、279、341、410	410

3.5.3 Implications for and Discussion on the Minimum Detectable Concentration

Substituting the simulated optimal detection efficiency ε = 71.90% into Eq. (1), and assuming representative operational parameters (background count rate n_b = 0.3 cps, achievable via coincidence measurement and shielding; counting time t_b = 3600 s; sample volume V = 0.010 m^3; and sample recovery rate η = 1), the calculated theoretical Minimum Detectable Concentration (MDC) is approximately 5.9 Bq/m^3.

This result can be contextualized against other established methods for Kr-85 monitoring. The German Federal Office for Radiation Protection operates conventional proportional counters with a typical limit of detection around 8 $mBq \cdot m^{-3}$ for Kr-85 [22]. Recently, Liang et al. reported an anti-cosmic ray internal gas proportional counter system achieving a minimum detectable activity of ~ 7 mBq for ^{85}Kr, corresponding to an MDC roughly three orders of magnitude lower than this work under comparable normalization [23]. The Low-level Automated Kr-85 Analyzing System (LAKAS) developed by Zeng et al. achieves an MDC of ~ 5 $Bq \cdot m^{-3}$, which is comparable to the present design but benefits from integrated gas chromatography[14]. At the extreme high-sensitivity end, atom trap trace analysis enables single-atom level detection, albeit with significantly greater system complexity and cost [4].

Each established method carries inherent limitations that motivate alternative approaches. Liquid scintillation counting, while sensitive, involves discontinuous operation and offline analysis [7]. High-purity germanium gamma spectrometry, used in routine monitoring, suffers from high MDCs (tens of thousands of Bq/m^3) due to the weak gamma branch of Kr-85 [14]. Conventional internal gas proportional counters require stringent gas purity and elaborate purification systems [24]. Atom trap

trace analysis, despite its revolutionary sensitivity, is confined to laboratory settings due to its complexity [4].

Against this backdrop, the PSFA design presented here offers a compact, solid-state platform with moderate sensitivity. It occupies a niche between laboratory-grade high-sensitivity systems and simpler screening methods, analogous to how polished fiber interfaces balance optical performance against fabrication feasibility.

In summary, this section has clarified the influence mechanisms of key structural parameters on detection efficiency through systematic Geant4 Monte Carlo simulations and has identified an optimized parameter set that maximizes system performance. The simulation results demonstrate that the proposed PSFA detector scheme achieves high theoretical detection efficiency for Kr-85. Its compact and efficient design establishes a solid physical foundation for the development of a new type of portable, field-deployable Kr-85 monitor.

4. Conclusion and Prospects

This study systematically optimized the structural parameters of a plastic scintillating fiber array (PSFA) detector for the field monitoring of Kr-85 in gaseous effluents from nuclear facilities, using the Geant4 Monte Carlo simulation method. The key finding is that omitting the conventional PMMA cladding, employing surface-polished bare plastic scintillating fibers, and optimizing the fiber geometry and array arrangement can significantly enhance the system's detection efficiency for Kr-85 β particles. The specific optimized parameters are as follows: 410 bare fibers, each 640 μm in diameter and 40 mm in length, arranged in a circular pattern with an axial spacing of 1.12 mm. Under this configuration, the theoretical detection efficiency for Kr-85 reaches 71.90%. This result demonstrates the high signal-collection capability of the design at the physical level. Achieving high efficiency with a relatively small sample volume (about 10 L) highlights the detector's compactness and high-performance characteristics, providing a simulated and optimized physical basis for developing portable, field-deployable monitors for environmental Kr-85.

In practical applications, non-ideal factors such as gas-flow uniformity and potential adsorption of Kr-85 on the fiber surfaces should be considered. Non-uniform flow or local stagnation inside the detection chamber could reduce the spatial homogeneity of the source distribution, while surface adsorption may affect the response at low concentrations. Although not included in the present idealized model, these effects can influence measurement accuracy and stability and therefore require quantitative evaluation and compensation in the engineering implementation.

Future work based on this simulation may involve more comprehensive modeling, for example, incorporating realistic background radiation fields and material-property uncertainties, to better bridge the gap between simulation and actual performance. The optimized parameter set offers a valuable starting point for subsequent engineering development.

Declarations

Declaration of competing interest

The authors declare that they have no known competing financial interests or personal relationships that could have appeared to influence the work reported in this paper.

Author Contribution

Author Contributions StatementBin Huang: Conceptualization, Methodology, Software, Formal analysis, Investigation, Writing – Original Draft.Gui-Ying Guo: Methodology, Validation, Investigation, Resources.Yan-Jun Huang: Supervision, Project administration, Writing – Review & Editing.Jian-Lin Yao: Methodology, Formal analysis, Investigation.Qiang-Lin Wei: Validation, Data Curation.Shenging Chen: Software, Formal analysis, Investigation.Xue-Dong He: Formal analysis, Investigation.Yi-Bao Liu: Supervision, Writing – Review & Editing.All authors have read and agreed to the published version of the manuscript.

Acknowledgments

This work was supported by the National Key R&D Program of China (Grant No. 2023YFF0716300) and the CGN Peak Plan Project entitled "Online Monitoring System for Effluents Based on Nuclide Analysis".

Data Availability

The data generated and analyzed during this study are included in this published article. All simulation parameters, configurations, and results are described in the text or presented in the figures and tables.

References

1. Kondev F, Wang M, Huang W, Naimi S, Audi G (2021) The NUBASE2020 evaluation of nuclear physics properties. Chin Phys C 45:030001
2. Ahlswede J, Hebel S, Ross JO, Schoetter R, Kalinowski MB (2013) Update and improvement of the global krypton-85 emission inventory. J Environ Radioact 115:34–42
3. Kalinowski MB, Sartorius H, Uhl S, Weiss W (2004) Conclusions on plutonium separation from atmospheric krypton-85 measured at various distances from the Karlsruhe reprocessing plant. J Environ Radioact 73:203–222
4. Chu Y-Q, Wang W-H, Dong X-Z, Gao C, Gu J-Q, Hu S-M, Jiang W, Liu S-Y, Lu Z-T, Ritterbusch F (2023) Online monitoring of atmospheric krypton-85 with hourly time resolution. J Anal At Spectrom

38:1238–1243

5. Marie-Luce R, Mai P, Lerouge F, Cheref Y, Pierre S, Sabot B, Chaput F, Dujardin C (2024) Real-time detection and discrimination of radioactive gas mixtures using nanoporous inorganic scintillators. Nat Photonics 18:1037–1043
6. Huang Y-J, Guo G-Y, Chen C-F, Yang L-T, Shang-Guan Z-H, Sha X-D, Yao J-L, Hu C (2020) Automated separation and analysis of krypton-85 from low-volume gaseous effluent of nuclear power plant. J Radioanal Nucl Chem 323:213–222
7. Momoshima N, Inoue F, Sugihara S, Shimada J, Taniguchi M (2010) An improved method for 85Kr analysis by liquid scintillation counting and its application to atmospheric 85Kr determination. J Environ Radioact 101:615–621
8. Currie L, Klouda G (2001) Detection and quantification capabilities for 85Kr with the NIST low-level gas counting system: Impacts of instrumental and environmental backgrounds. J Radioanal Nucl Chem 248:239–246
9. Hartwig ZS, Gumplinger P (2013) Simulating the optical physics of nonlinear scintillation detectors with Geant4. Nuclear Instruments and Methods. Phys Res Sect A 737:155–162
10. Allison J, Amako K, Apostolakis J, Araujo H, Dubois PA, Asai M, Barrand G, Capra R, Chauvie S, Chytracek R (2006) Geant4 developments and applications. IEEE Trans Nucl Sci 53:270–278
11. Cheng W, Liang J, Wang L, Liang Y, Shi S, Zou L, Yang J, Guo Z (2026) Optimized simulation research of a plastic scintillation fiber array tritium detector in water. J Environ Radioact 291:107833
12. Li Q, Chu S, Xia B, Shuai M (2025) Development of continuous measurement technology for low-concentration gaseous tritium based on solid scintillation fiber. J Instrum 20:P05028
13. Yusoff R (2019) Development of a Radiation Counting System Based on a Plastic Scintillator for Medical Applications. University of York
14. Zeng J, Xiang Y, Luo F, Zhang C, Wu X, Xiang Q, Hao F, Ze R (2021) Development of a well-type phoswich detector for low concentration Krypton-85 measurement. Nuclear Instruments and Methods in Physics Research Section A: Accelerators, Spectrometers. Detectors Assoc Equip 1013:165634
15. Agostinelli S, Allison J, Amako Ka, Apostolakis J, Araujo H, Arce P, Asai M, Axen D, Banerjee S, Barrand G (2003) Geant4—a simulation toolkit. Nuclear instruments and methods in physics research section A: Accelerators. Spectrometers Detectors Assoc Equip 506:250–303
16. Allison J, Amako K, Apostolakis J, Arce P, Asai M, Aso T, Bagli E, Bagulya A, Banerjee S, Barrand G (2016) Recent developments in Geant4. Nuclear instruments and methods in physics research section A: Accelerators. Spectrometers Detectors Assoc Equip 835:186–225
17. Zhu J, Fang M, Wang J, Wei Z (2017) Timing window and optimization for position resolution and energy calibration of scintillation detector. Proceeding of IBIC:372–375
18. Bensong P, Zhiyong W, Zhen W, Qingwei Z, Junhao Y, Xiaoming T (2017) The coincidence test of the double-end output plastic scintillation detector

19. Currie LA (1968) Limits for qualitative detection and quantitative determination. Application to radiochemistry. Anal Chem 40:586–593
20. Cheng W, Zeng L, Zhou H, Liang J, Deng K, Zhang Q, Liu W (2025) Feasibility analysis of tritium measurement in the aqueous medium based on a plastic scintillating fiber array. Nucl Technol 211:500–512
21. Xu R-Y, Dong C-H, Mao X-Q, Zhang Q-X, Gong H, Liao K-y, Lu Z-G, Ge L-q, Gao Z-Y, Luo T-F (2021) Simulation results of the online tritiated water measurement system. Nucl Sci Tech 32:126
22. Schlosser C, Bollhöfer A, Schmid S, Krais R, Bieringer J, Konrad M (2017) Analysis of radioxenon and Krypton-85 at the BfS noble gas laboratory. Appl Radiat Isot 126:16–19
23. LIANG J, XIE F, DAI Y, SHI Q, WANG C, LI X, GUAN Q, JIANG W, LIU YUG Z (2025) Radioactivity Measurement of 85 Kr by Using Anti-cosmic Ray Internal Gas Proportional Counter. At Energy Sci Technol 59:1120–1125
24. Chen C-F, Yang L-T, Huang Y-J, Shang-Guan Z-H, Guo G-Y, Yao J-L, Sha X-D (2020) A study on 85Kr measurement with an internal gas proportional counter. Appl Radiat Isot 155:108948

Figures

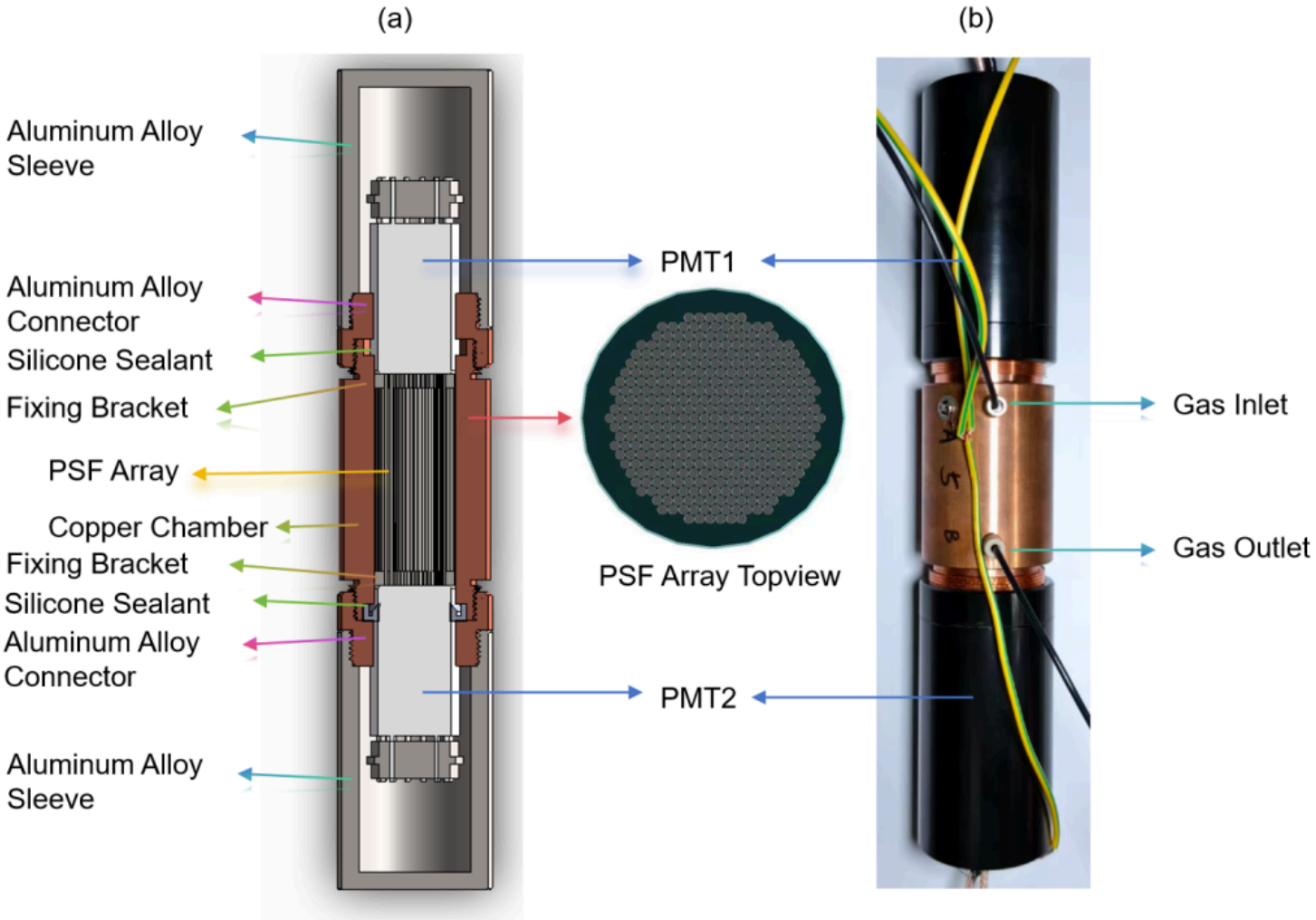


Figure 1

Detector structure: (a) simulation model; (b) photograph of the prototype.

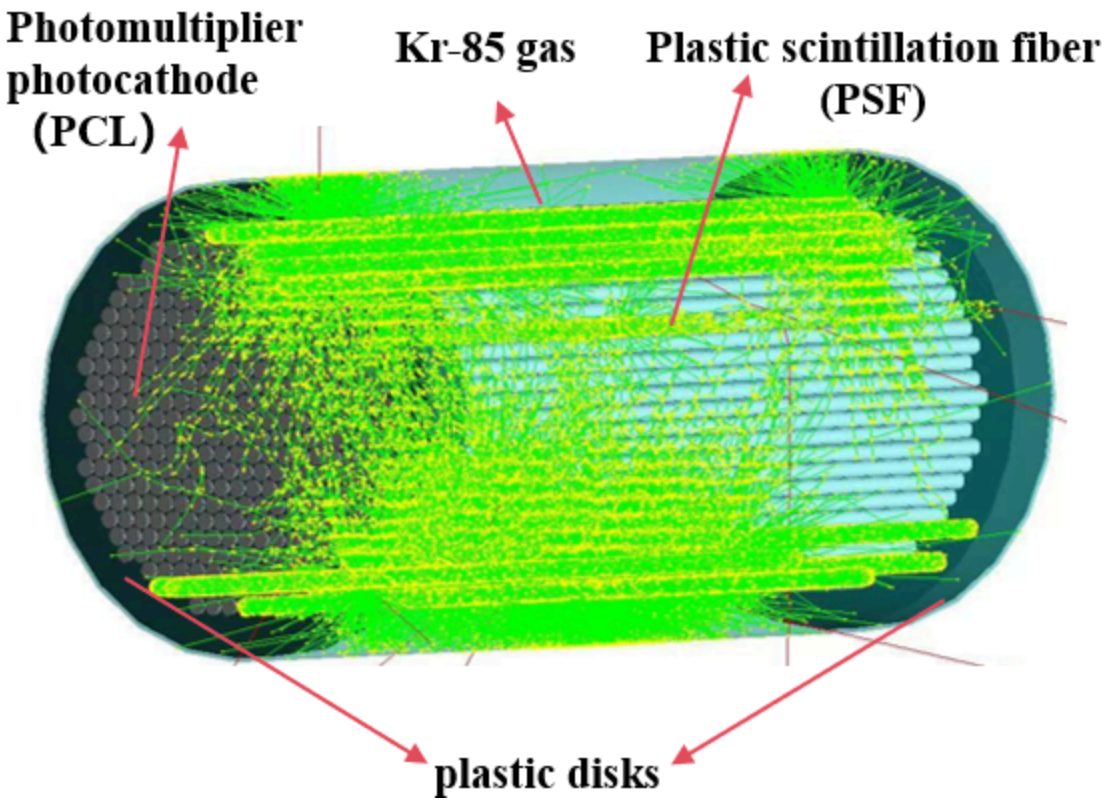


Figure 2

Schematic of the basic simulation model.

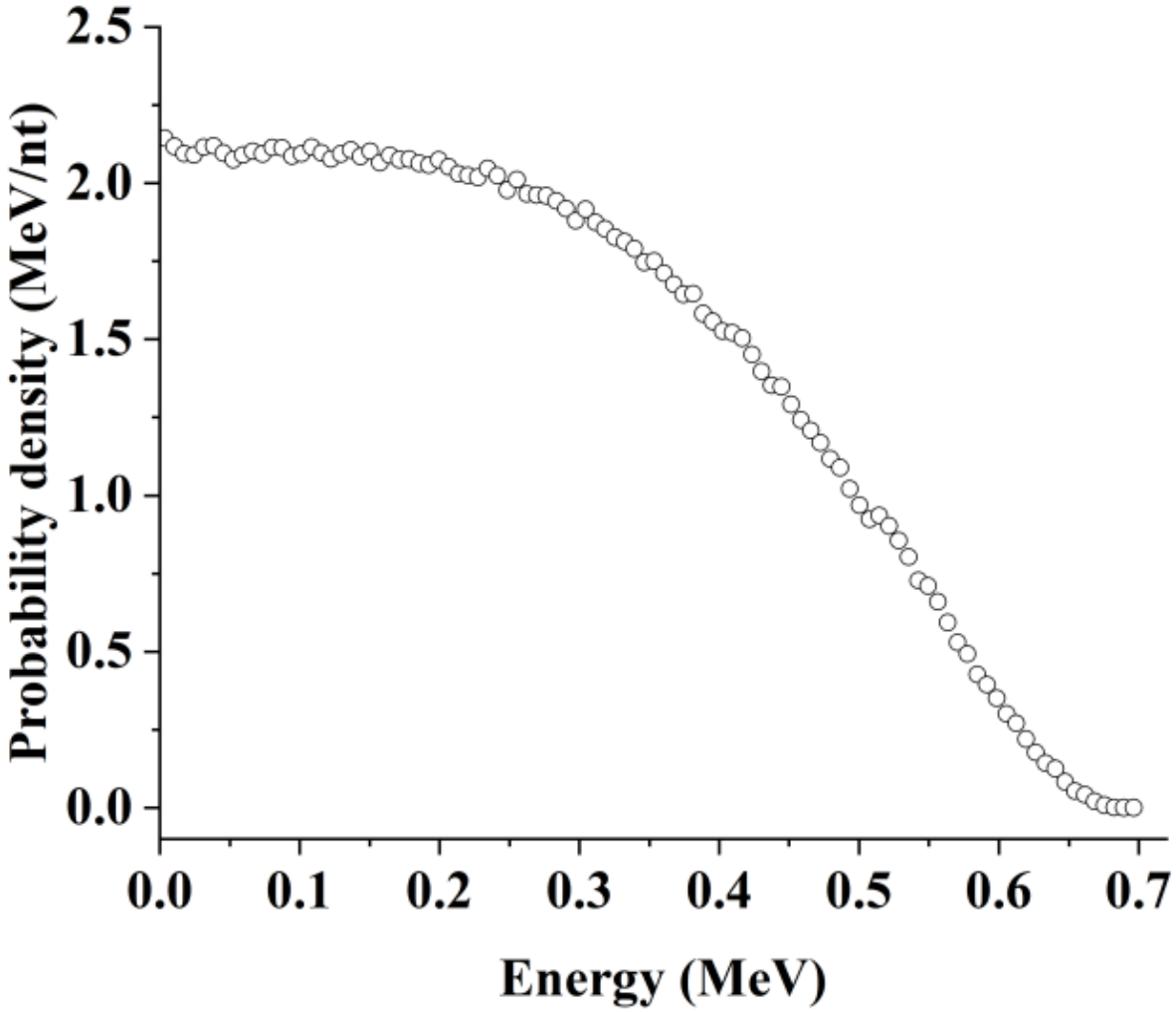


Figure 3

Simulated energy spectrum of Kr-85 β particles.

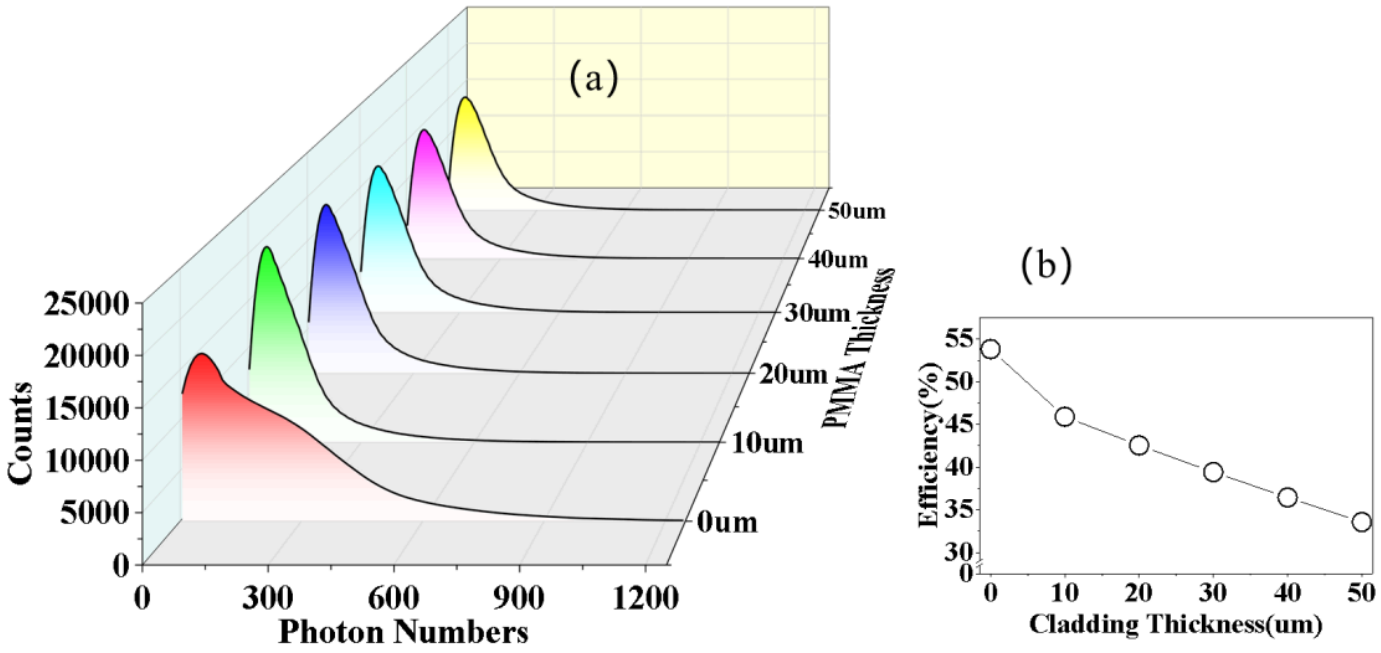


Figure 4

Variation of detection efficiency with PMMA cladding thickness: (a) simulated photon distribution and (b) efficiency trend.

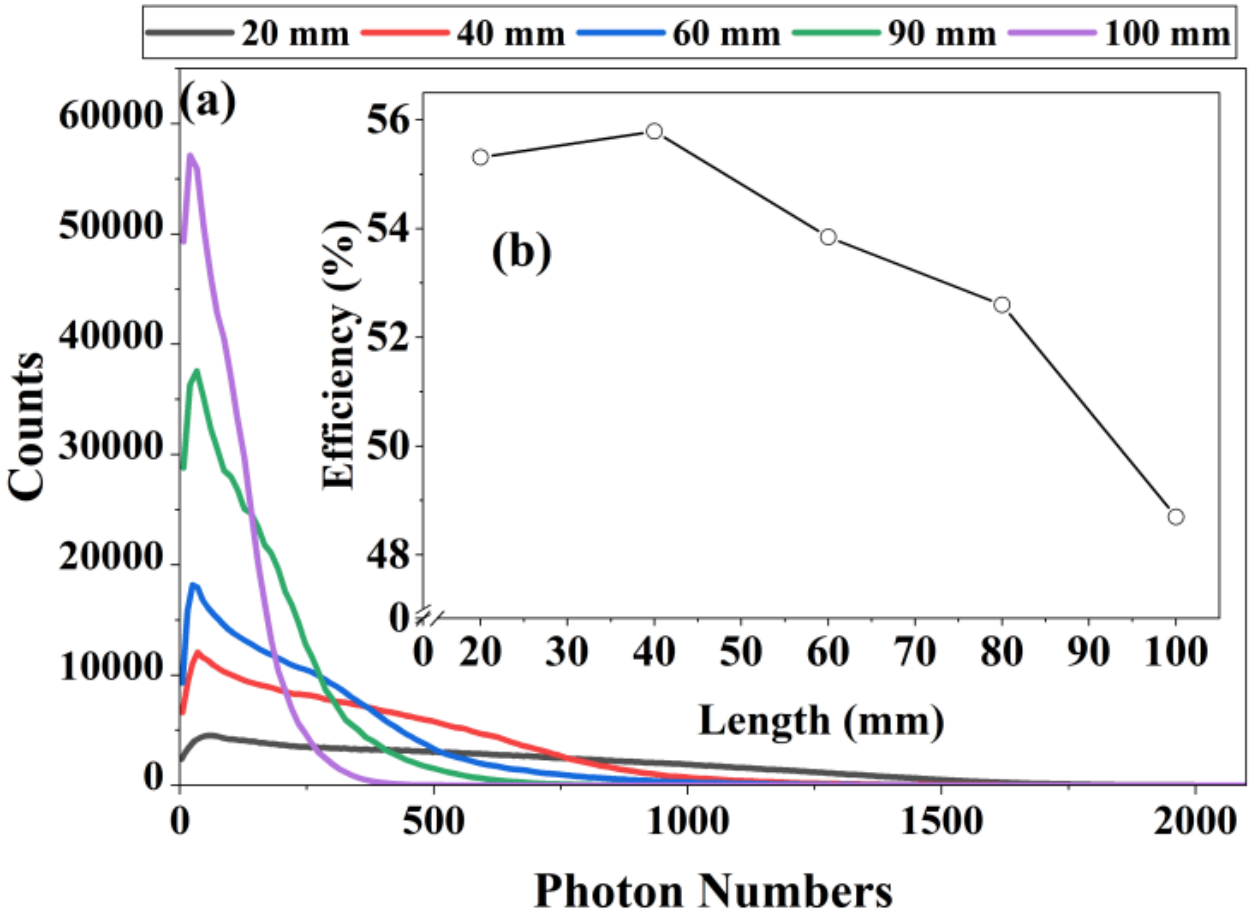


Figure 5

Variation of system detection efficiency with fiber length: (a) effective coincidence photon spectra; (b) efficiency as a function of length.

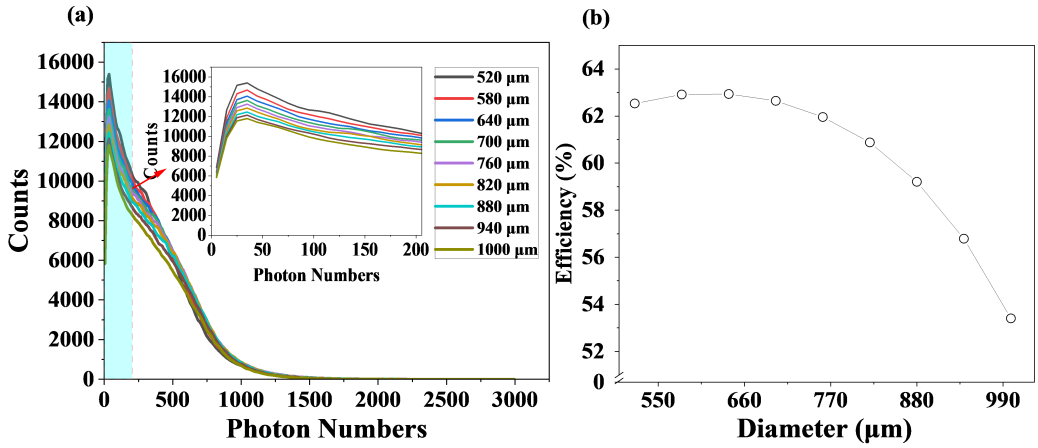


Figure 6

Relationship between detection efficiency and fiber diameter: (a) simulated photon distribution; (b) efficiency variation.

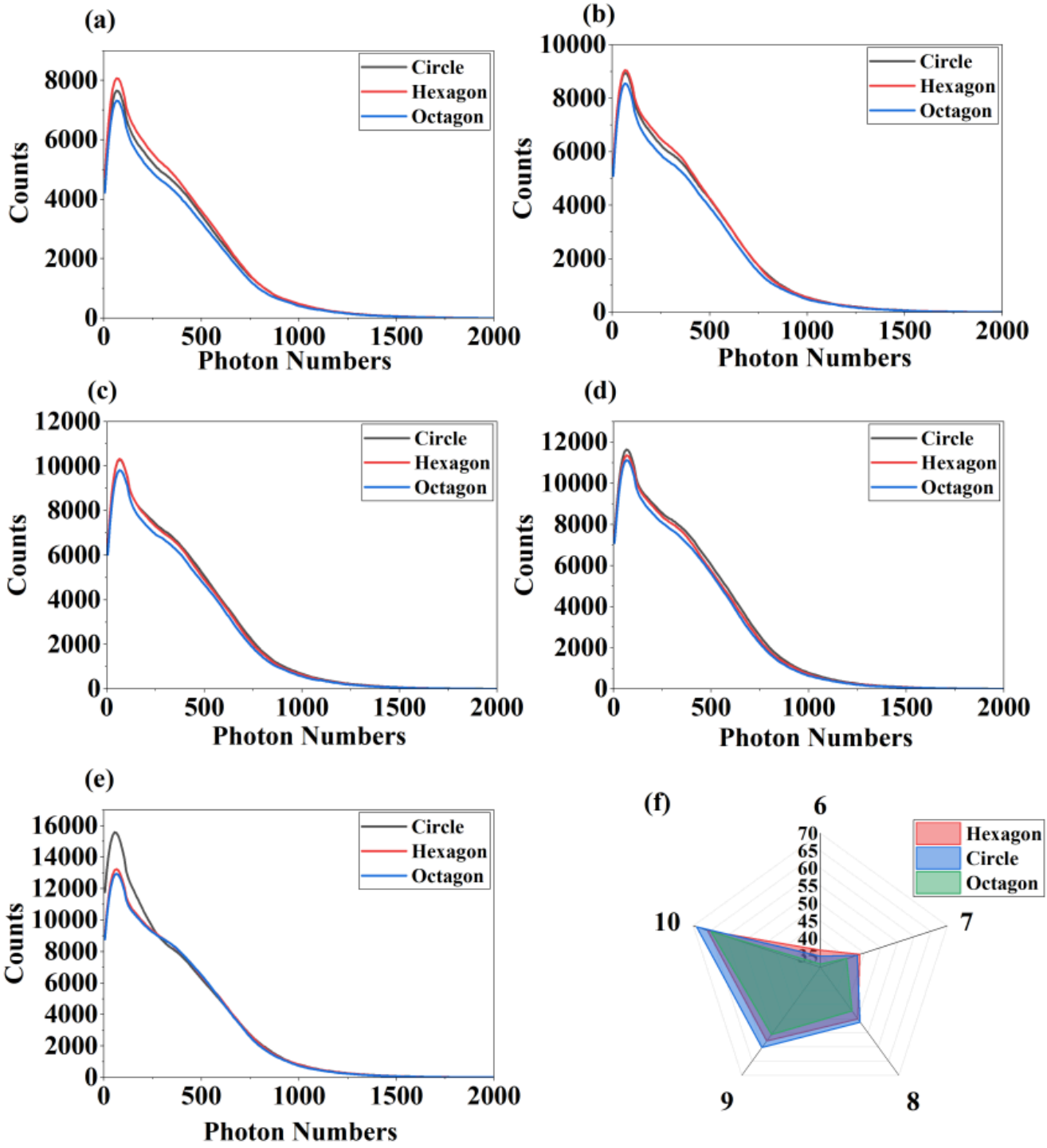


Figure 7

Variation of detection efficiency with fiber-array pattern and layer number: (a–e) effective coincidence photon spectra for 6–10 layers; (f) detection efficiency for different patterns and layer numbers.

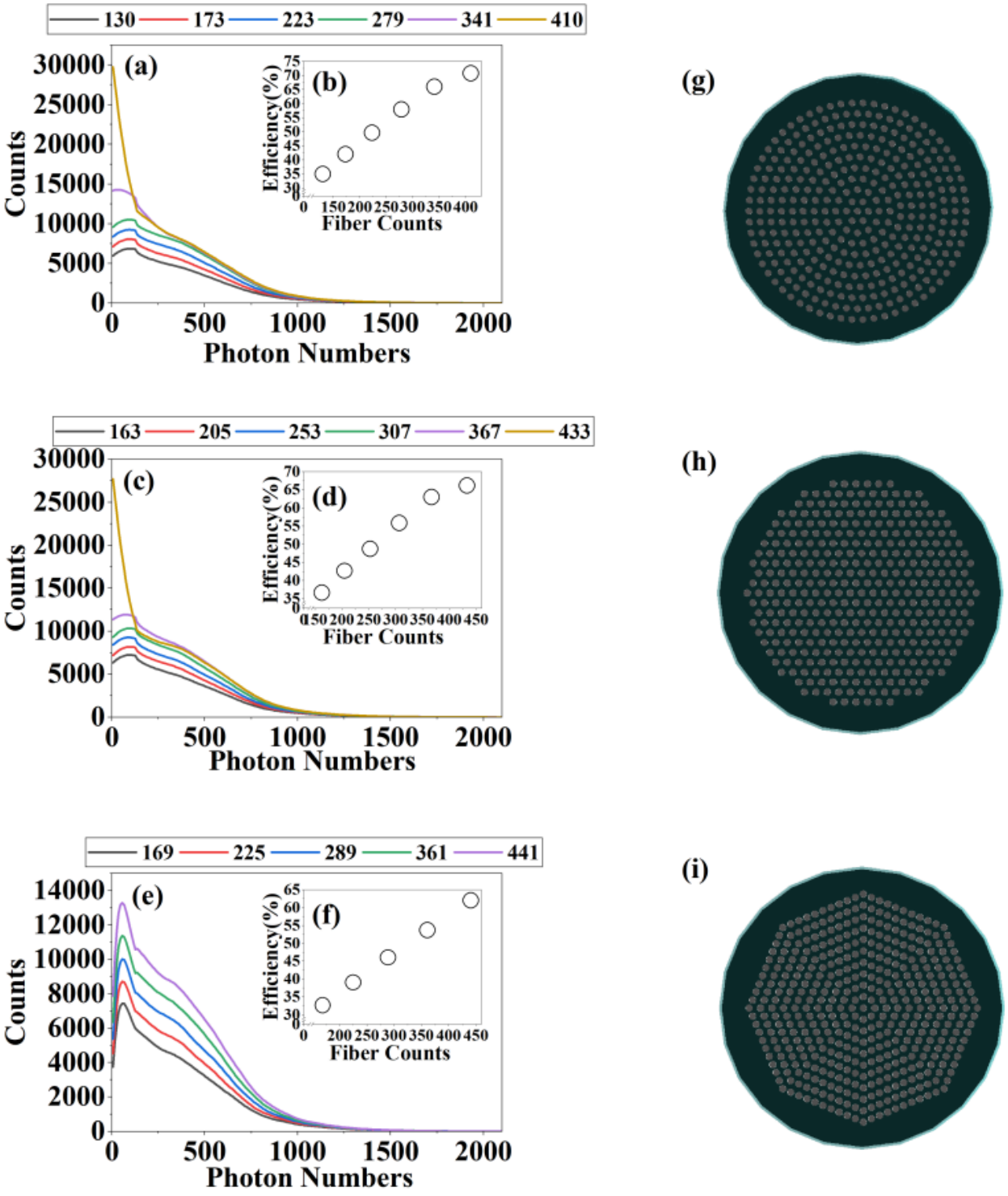


Figure 8

Variation of detection efficiency with fiber count and array pattern: (a, c, e) effective coincidence photon spectra; (b, d, f) detection efficiency as a function of fiber count for circular (a, b), hexagonal (c, d), and octagonal (e, f) arrangements; (g–i) schematic layouts of the three patterns with different fiber counts.

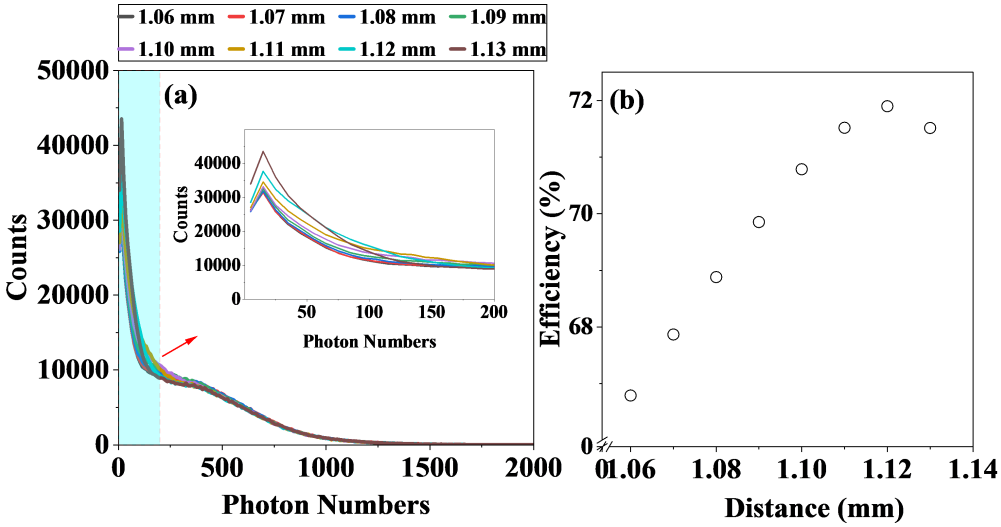


Figure 9

Variation of detection efficiency with fiber spacing: (a) effective coincidence photon spectra for spacings of 1.06–1.13 mm (inset: enlarged view of the low-photon-count region); (b) detection efficiency as a function of fiber spacing.